Journal Pre-proofs

Experimental and numerical investigation on in-plane impact behaviour of chiral auxetic structure

Dianwei Gao, Shuhong Wang, Mingzhong Zhang, Chunwei Zhang

Please cite this article as: Gao, D., Wang, S., Zhang, M., Zhang, C., Experimental and numerical investigation on in-plane impact behaviour of chiral auxetic structure, *Composite Structures* (2021), doi: https://doi.org/10.1016/j.compstruct.2021.113922

This is a PDF file of an article that has undergone enhancements after acceptance, such as the addition of a cover page and metadata, and formatting for readability, but it is not yet the definitive version of record. This version will undergo additional copyediting, typesetting and review before it is published in its final form, but we are providing this version to give early visibility of the article. Please note that, during the production process, errors may be discovered which could affect the content, and all legal disclaimers that apply to the journal pertain.

Experimental and numerical investigation on in-plane impact behaviour of chiral auxetic structure

Dianwei Gao [a,b], Shuhong Wang [b], Mingzhong Zhang [c], Chunwei Zhang [a,*]

[a] School of Civil Engineering, Qingdao University of Technology, Qingdao, 266033, China

[b] College of Resources and Civil Engineering, Northeastern University, Shenyang, 110819, China

[c] Department of Civil, Environmental and Geomatic Engineering, University College London, London, WC1E 6BT, UK

Corresponding author: Chunwei Zhang; E-mail address: zhangchunwei@qut.edu.cn

Abstract: This paper presents an experimental study on impact behaviour and plastic evolution of chiral structure subjected to in-plane impact loading using a Split Hopkinson pressure bar (SHPB). The finite element (FE) model developed in ABAQUS/Explicit was validated and utilized for parametric study, and further developed as an extension of experimental work. The impact scenarios from both structure itself and external input are considered, including relative density, topology parameter r/R and initial impact energy. Results indicate that chiral structure exhibits three critical failure modes corresponding to various impact velocities ranging from 5 m/s to 50 m/s. Interestingly, chiral structure occurs with two densification stages induced by ligaments-dominated and nodes-dominated crushing deformation, respectively, proving the capability of independent energy management mechanism. Increasing the value of relative density from 0.19 to 0.39 contributes to a maximum of 250% increase in the specific energy absorption (SEA). Although increasing the value of r/R from 0.04 to 0.2 can dramatically decrease *Poisson's ratio* (PR) from 0.07 to -0.63 (significant negative PR), high strain-rate dependence of PR is also observed. In addition, the impact displacement is mostly influenced by initial impact energy but not by impact velocity and mass. The obtained results of this study provide a new insight into the impact performance of chiral structure, which contributes to the optimal design of auxetic crashworthiness system.

Keywords: Chiral structure; Auxetic structure; Negative Poisson's ratio; Impact; Split Hopkinson pressure bar.

1. Introduction

Lightweight cellular structures have been widely used for structural protection against impact or blast loads benefiting from the excellent energy absorption capabilities and high strength-to-weight ratio. The energy absorption mechanism of these lightweight structures such as honeycombs, foams and lattice structures usually attribute to the progressive crushing failure of the thin wall or the ligaments. Among various lightweight cellular structures, conventional honeycomb structures are widely used as core components in composites constructions for a variety of industrial applications such as in the automotive industry, aerospace industry and marine industry. At length, a sufficient number of studies on the in-plane compressive behaviours [1-8] and the out-of-plane compressive behaviours [9-18] of hexagonal honeycomb structures have been investigated considering both quasi-static and dynamic scenarios. By conveniently changing the geometry shape of honeycomb unit cells, e.g., tuning the interior angles of hexagonal honeycomb to be concave, re-entrant auxetic honeycomb can be obtained with unique deformation feature characterised by negative Poisson's ratio (NPR) [19-21]. This particular structural behaviour can result in unique deformation modes and energy absorption mechanisms from convention hexagonal honeycombs, and thus provide opportunities to change structural mechanical properties by just changing the cell microstructures [22]. In the last decades, the

NPR materials have attracted much attention in the research field of impact and blast resistance.

Materials exhibiting unexpected and counter-intuitive NPR characteristics, also known as 'auxetic materials' or 'auxetics' termed by Evans et al. [23], are capable of shrinking in the transverse directions when compressed in the longitudinal direction. Similarly, when they are stretched in the longitudinal direction, they expand in the perpendicular width-wise directions. It is known that isotropic materials satisfy the relationship: $G = 3K(1-2v)/[(2(1+v))]$, where G is shear modulus, K is bulk modulus. Hence, $1+v \rightarrow 0$ as $v \rightarrow -1$, it is known that the typical deformation behaviour of NPR materials will trigger enhanced shear modulus compared to non-NPR materials. As we also know that the indentation resistance of isotropic materials improves proportionally with the increasing ratio of materials' Young's modulus E to $1-v^2$ [24], the materials with NPR in the range of $-1 \leq v < -1/2$ will possess enhanced indentation resistance compared to non-NPR materials when they have the same value of E [25]. Additional merits have also been observed in NPR materials such as fracture toughness, synclastic curvature, crushing energy absorption, wave guidance, deploy-ability, thermo-auxeticity and mechanical impedance [26-33]. Owing to the unique deformation features and great mechanical potential, a number of applications would include, e.g., sports protective equipment, biomedical devices, fasteners, nails and rivets, smart filters and sensors, auxetic cushion seats and protective textiles based on the concept of auxetic materials have sprung up in the past couple of years, even though some of these are proposed tentatively. Literature review [34-42] on auxetic materials has been sufficiently carried out witnessing the development of auxetics over the past twenty years. However, a large amount of literature has been published on the studies of elastic mechanical properties [43-45] of auxetic materials under static and dynamic loading.

The auxetic materials profiting from the counter-intuitive deformation law has also been demonstrated that it can contribute to improved performance in energy absorption against compressive loading, for example, in impact and blast scenarios. The re-entrant auxetics in both 2D and 3D configurations are the most discussed NPR materials used in structural protection to date. Liu et al. [26] numerically conducted a comparative study between conventional hexagonal and re-entrant honeycomb in terms of deformation mechanism, impact force and energy absorption capacity. It was found that the NPR effect contributed to more plastic energy dissipation but resulted in higher impact stress. Imbalzano et al. [46] carried out a numerical investigation on the blast resistance of sandwich panels with auxetic cores. It was noticed that auxetic composite panels were more effective in impulsive energy absorption, displacement and velocity attenuation of the back facets in comparison with the monolithic ones. Wu et al. [47] proposed a graded design of re-entrant structures which could exhibit enhanced energy absorption under both low-speed and high-speed impact. Logakannan et al. [48] investigated the dynamic crushing of a 3D re-entrant structure by both experimental and numerical methods, and it was found that the specific energy absorption (SEA) of which was not superior compared with other cellular materials such as foams and honeycombs although the density was tunable over a wide range. Experimental and numerical investigations on foam-filled re-entrant cellular structures were conducted by Yu et al. [49], and the benefits such as higher specific energy absorption and possible reversible deformation were obtained. In addition, the energy absorption capacity of other auxetic structures such as helical yarns[50], arrowhead honeycomb [5, 51] and auxetic foam [52-54] has also been less studied. Since the above studies are among the first on topic of structural crashworthiness assessment, a limited number of auxetic structures have been covered. Hence, there is insufficient data to develop a comprehensive understanding of the effectiveness of NPR merits in practical application. Meanwhile, although auxetics have drawn a lot of attention in academia and business, and much efforts have been made aiming to invigorate the application of auxetics, finding solutions to the technical issues such as the improvement of mechanical strength, reliable repetitive and batch manufacturing are still the challenges faced by the researchers in pursuing the practical application of auxetics.

Chiral auxetic structures exists an NPR effect undergoing in-plane deformation, which was first implemented by Lakes et al. [55] in 1991. The in-plane layout of the chiral structure depends on the key

geometric parameters of the nodes and ligaments, as shown in Fig. 1. Every six ligaments of length *L* are tangentially attached to one node of radius *r*. The distance between adjacent nodes is *R*. The wall thickness of nodes and ligaments is t_n and t_l, respectively. The angle between adjacent ligaments and the angle between tangential line and node centre line is 2ϑ and β. The in-plane and out-of-plane mechanical properties of chiral lattices in the elastic range have been elaborated systematically by Spadoni et al. [56-58]. The elastic constants of structures in chiral family including uniaxial stiffness, Poisson's ratio, shear modulus and buckling strength have also been measured by other researchers [43, 44, 59-64]. Gao and Zhang [65] performed the first numerical and theoretical study on the in-plane impact performance of chiral structure, and the research findings indicated that chiral lattices dissipated plastic strain energy in two stages: ligaments buckling and nodes buckling under the low-speed impact. This merit of unique energy storage mechanism motives us to design a crashworthiness system in which one part of the structure experiences irreversible plastic deformations in the wake of impact while the other part can still remain intact. However, to the authors' knowledge, comprehensive experimental study and further discussion on the plastic energy management of chiral structure at different stages are not reached.

To this end, this study aims to investigate the impact behaviour, failure mode and energy absorption mechanism of chiral auxetic structure by both experiments and numerical simulations. The experimental work is implemented with the aid of Split-Hopkinson pressure bar (SHPB) and Digital Image Correlation (DIC) technique. This could capture the deformation process and strain evolution of specimen under impact loading. In order to reduce the boundary effect in the experiments and prepare for the parametric study, a finite element (FE) model was developed by means of commercial FE analysis software ABAQUS 6.14-4 (SIMULIA™ by Dassault Systèmes®) and validated against the dynamic test results in terms of force histories. Subsequently, the validated FE model was used to explore the effects of relative density ($\overline{\rho}$), topology parameter *r/R*, initial impact velocity (v_i) and initial impact mass (m) on the crashworthiness parameters of chiral structure such as specific energy absorption (SEA), crush force efficiency (CFE), cushion factor (CF) and Poisson's ratio (PR). The obtained results could offer insights into the appropriate design of crashworthiness system using chiral structures.
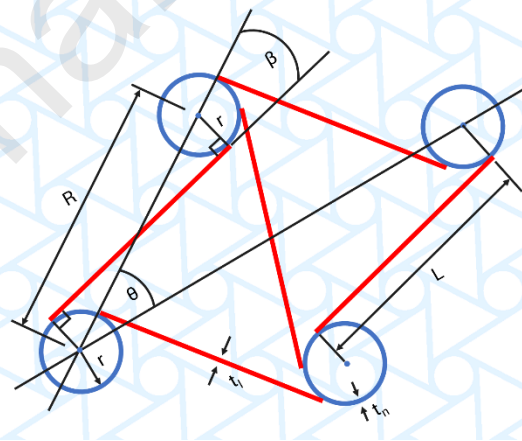

Fig. 1. Geometric parameters of chiral unit cell.

2. Experimental program

In this section, the design of experimental tests for auxetic structures will be described in terms of dynamic compression test. Moreover, the capability of the ABAQUS/Explicit models to accurately simulate the impact behaviour of auxetic structures undergoing compressive loads will be assessed against the experimental results.

2.1. Materials and specimen preparation

The specimens have been obtained by cutting cylinders and equilateral triangular prism from the aluminium alloy panel using an ultra-high pressure water-jet machine. The aluminium alloy is labelled as A5052 and has the Young's modulus of 70 GPa, Poisson's ratio of 0.3, yield stress of 130 MPa and density of 2.7 g/cm³ (as presented in Table 1). All the specimens with a dimension of 70 mm × 70 mm in the plane and 30 mm in depth were made for dynamic crushing tests. To prepare the digital image correlation (DIC) specimens, the surface of specimens for dynamic testing was processed by spraying black paint on the white painted surface to obtain the random speckles. It should be noted that the specimens loaded in the present experiments just represent one of the collapse mechanisms possibly exhibited for the chiral structure under in-plane impact because of the limitation of specimen size from the available experimental condition. The radius r and distance R between the two circle centres of adjacent nodes were 5 mm and 25 mm, respectively, as shown in Fig. 2. The ligaments and nodes of the designed specimens were taking the same thickness of $t_l = t_n = 4$ mm. According to designated geometric topology, the relative density of the used chiral structure was obtained to be $\bar{\rho} = 0.83$. It should also be underlined that this magnitude of relative density $\bar{\rho}$ cannot guarantee a fully bending deformation mechanism of the ligaments conformed to the theoretical model proposed by Prall and Lakes [55]. The effect of relative density $\bar{\rho}$ on the mechanical response and energy absorption of the chiral structure in in-plane direction has also been discussed in this paper.
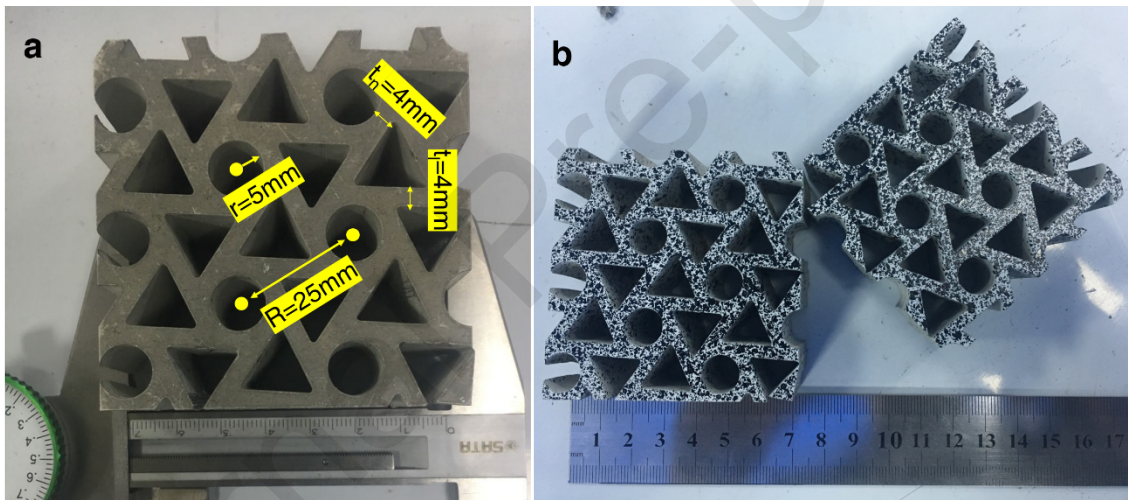

Fig. 2. Specimens used for dynamic tests. a) Key parameters of chiral structure, where r = 5 mm, R = 25 mm, t_l = t_n = 4 mm. b) Speckle pattern for DIC.

2.2. Test method

The DI-HPB (Direct impact Hopkinson pressure bar) dynamic tests have been carried out to obtain the failure modes and assess the crashworthiness of chiral structure. The experimental data will also be used to validate the numerical model developed in the following section.
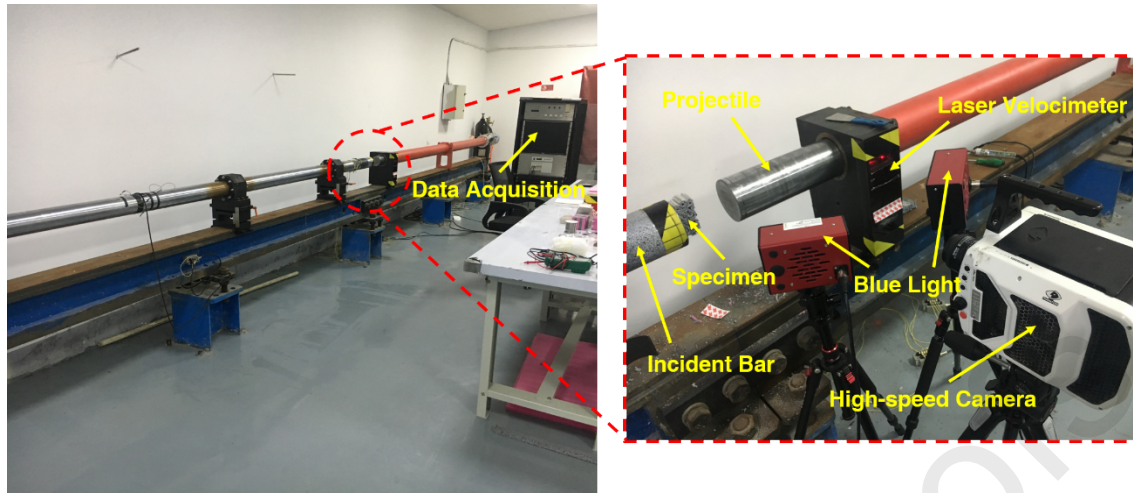
Fig. 3. Setup for dynamic DI-HPB tests.

Crashworthiness assessment of chiral structure under dynamic loading has been conducted with the aid of the Split Hopkinson Pressure Bar (SHPB) apparatus which consists of five major components (i.e., see the image in Fig. 3): loading system (a gas gun equipped commonly), incident bar, data acquisition system, laser speed device and high-speed camera. Then, the DI-HPB test is implemented using traditional SHPB apparatus, but the specimens are attached directly on the top surface of the incident bar instead of sandwiching the specimens between the incident bar and transmission bar. The projectile will strike the specimens directly. The strain gauge installed on the incident bar will record the stress variations and assist in investigating the cushioning effect of the attached chiral structures. Fig. 4 shows the customised DI-HPB for the present study which has a projectile of 2 m in length, an incident bar of 6 m in length, a transmission bar of 6 m in length, and all the three cylindrical bars share the same size of the diameter of 100 mm in length. The specimen was attached to the frontal surface of the incident bar which is 110 mm far from the gas tube. The projectile and bars of DI-HPB are made of high strength alloy steel labelled 42CrMo which has the density and the elastic modulus of 7850 kg/m³ and 210 GPa (as listed in Table 1), respectively.
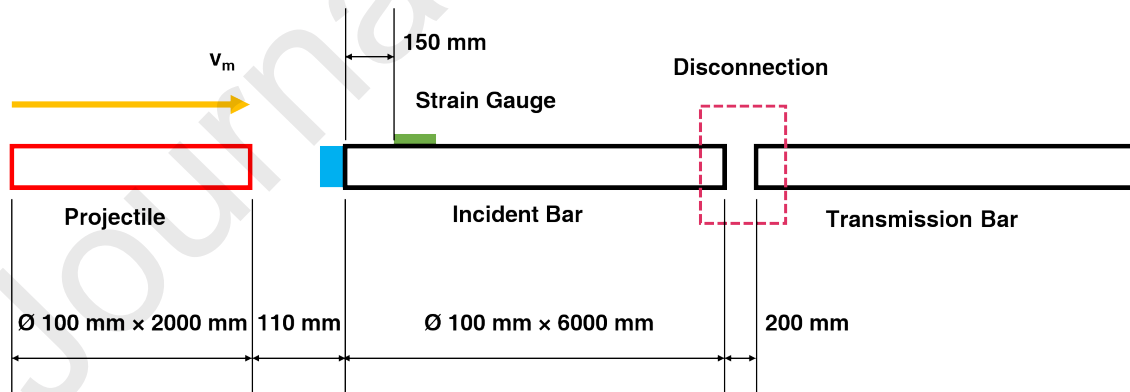

Fig. 4. Components and configuration of DI-HPB apparatus.

Table 1 Material properties used in DI-HPB test.

Material properties	Chiral Structure (5052 Aluminium)	Projectile & Bars (42CrMo Steel)
Young's modulus, E (GPa)	70	210
Poisson's Ratio, ν	0.3	0.3
Yield strength, σ_Y (MPa)	130	-
Density, ρ (g/cm^3)	2.7	7.85

The Wheatstone bridge has been used to measure the output voltage induced by the resistance changes of the 120 Ω strain gauge positioned 150 mm from the frontal surface of the incident bar. The incident bar and transmission bar were disconnected, and there is a space of 200 mm length between these two bars. The projectile, propelled by a gas gun, struck the specimens with velocities of v_m=2.36 m/s and v_m = 8.43 m/s. The present range of velocities represents the low-speed and high-speed impact, respectively. Laser speed device was used to measure the speed of the projectile in each test.

In order to capture the full course of dynamic crushing, the digital imaging correlation (DIC) technique was applied to obtain the strain fields through analysing the photos which were recorded using a high-speed camera (Phantom v2511) which was kept at a sample rate of 68,000 fps. Meanwhile, the speed of projectile before the contact with the specimen and the speed of the incident bar after the impact can also be obtained by taking photos. The blue lights have also been used to help get higher-resolution data and lower noise.

Then, the impact characteristics of chiral structures subjected to low-speed and high-speed strike were investigated by DI-HPB tests so as to evaluate how the presence of a chiral lattice structure mitigates the impact stress imposed on the protected structure (the incident bar referred in the present study). The experiments were also mimicked by numerical models. First, the DI-HPB tests were carried out in the absence of the chiral lattice structure attached at the surface of the incident bar, and two impact velocities of approximate 2.36 m/s and 8.43 m/s were considered in order to estimate the influences of partial deformation and full compression of the chiral structures on the impact response of the protected structures.

3. FE modelling

In order to ease the boundary effect and effectively identify the possibly different failure modes and deformation shapes of the chiral structures under impact loading, the chiral structures with the same ratio of L to R and the value of R as the specimen used in the experimental tests but with a larger in-plane dimension of 200 mm × 200 mm and an out-of-plane depth of 1 mm has been modelled. The ABAQUS/Explicit FE model setup for the in-plane compression of the chiral structure is shown in Fig. 5.
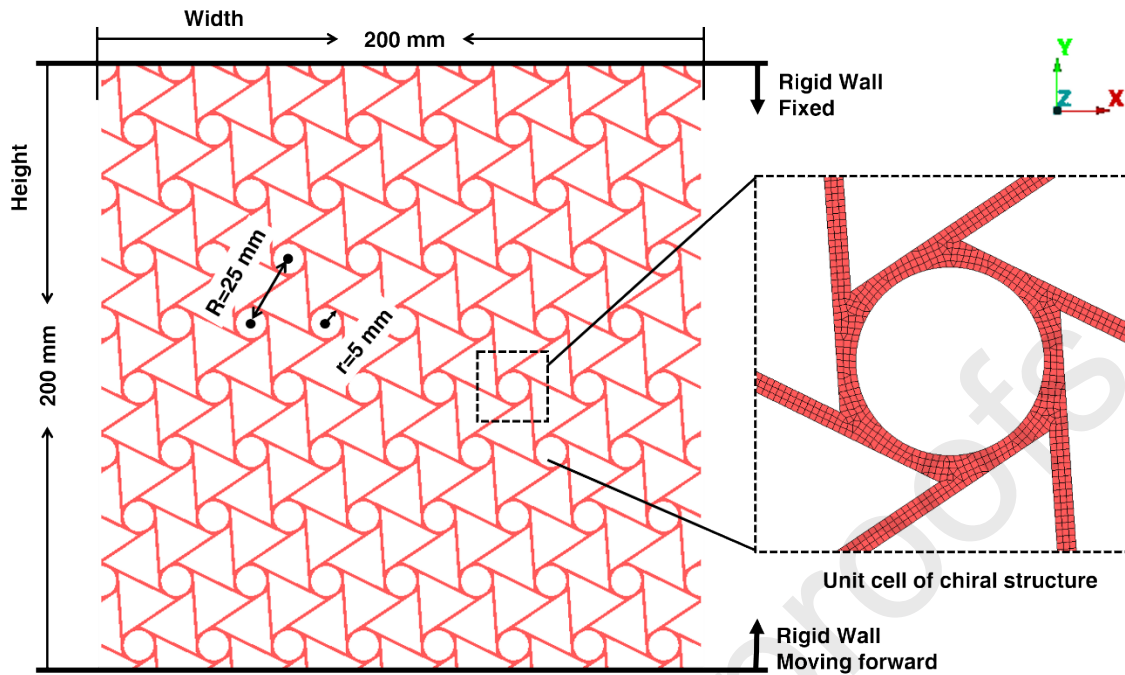
Fig. 5. Boundary condition for FE modelling of chiral structure under in-plane compression.

3.1. Material model and element selections

In this study, the elastic perfectly plastic material constitutive model was applied to emulate the aluminium alloy based chiral structure (details as listed in Table 1). This assumption has been proven to be reasonable in the simulation of impact behaviour of thin-wall aluminium structures such as hexagonal honeycombs [66], arrowhead honeycombs [5] and re-entrant honeycombs [26]. Although deformation modes of honeycomb structures are sensitive to impact velocity, the aluminium alloys itself have no obvious strain-rate effect under impact loads.

The chiral structures were modelled using solid elements of 6-nodes linear triangular prism (C3D6) and 92.4% 8-nodes linear brick (C3D8R) with reduced integration and default hourglass control algorithm. The rigid walls were modelled using shell elements of S4R. The FE model was meshed with a global element size control. The basic principle of designating the side length is to ensure that at least three layers of solid elements were distributed along the thickness of ligaments and nodes.

3.2. Boundary conditions and contact algorithm

The top rigid wall was fixed at all six degrees of freedom (DoFs). The bottom rigid wall was constrained at the reference node which was allowed to travel only along the Y+ direction. The chiral structure was fixed at all nodes, including all translational and rotational DoFs in the out-of-plane direction. To avoid the initial penetration, the initial distance between chiral structure and top rigid wall and bottom rigid wall is assigned to be 0.05 and 0.15 mm, respectively.

Abaqus/Explicit provides two algorithms for simulating contact interactions among different parts in the numerical model i.e., the general contact algorithm and the contact pair algorithm [67]. The general contact algorithm, the default self-contact algorithm in ABAQUS/Explicit, was used in this study to automatically include all the possible contact interactions during the impact processes. In this algorithm, the penalty contact formulation was the enforced to introduce contact constraints between surfaces. The penalty stiffness enforcing a "hard" contact option was chosen automatically by the code. The coulomb friction model was used

to account for the frictional forces between contacting surfaces with a friction coefficient of 0.25.

3.3. Model validation

3.3.1. Size effect

In order to obtain a proper dimension of the FE model using the minimum number of the solid elements, the convergence analysis of the model size was conducted in terms of the crushing plateau stress. The plateau stress was calculated from the 10%-20% crushing strain of the chiral structures with the various structural dimensions ranging from 50 × 50 mm to 300 × 300 mm. These dimensions also represented the maximum possible number of unit cells 3 and 13 in both the width and height directions. Fig. 6 shows the relative error of the plateau stress corresponding to different dimensions and different number of unit cells of the FE models. The result shows that the relative error of the chiral structure model with the dimension of 200 × 200 mm (9 × 9 unit cells) can be controlled in 5%. And this sufficient large dimension of the chiral structure model was allowed to include all the deformation modes at different crushing strain.
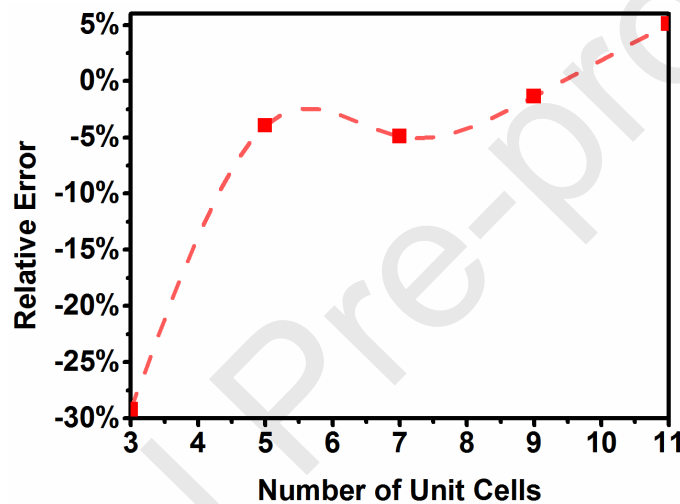

Fig. 6. Plateau stress of chiral structure with various numbers of unit cells.

3.3.2. Comparison with experimental results

To assess the capability of the ABAQUS/Explicit models in dynamic testing, the same impact process in the DI-HPB tests was simulated to obtain the whole deformation process of chiral structures at different levels of strain rates. Although the dimension of FE model in Fig. 5 is different from the specimen in the DI-HPB test, the same simulation methodology (element types and boundary conditions for chiral structure, principle for mesh generation and contact algorithm) as in Sections 3.1 and 3.2 was applied here. Fig. 7 shows the detailed numerical model setup in the DI-HPB experimental test. The impactor and incident bar were meshed well with pure hexahedral elements C3D8R. The element size for the solid part was approximate 1.3 mm of side length to ensure that at least three layers of solid elements were distributed along the thickness of ligaments and nodes. With such an FE mesh control, the discretisation of the 3D FE model resulted in 83,507 solid elements. No plastic behaviour was included in the material model for the projectile and bars because they did not show any sign of deformation during the impact test. The strain-rate sensitivity of the aluminium alloy chiral structures was also neglected in the current paper, which has been proven to be reasonable in most cases [68, 69]. To avoid the initial penetration between the chiral structure and steel bars, the initial distance between these parts is assigned to be 0.1 mm. The projectile struck the chiral structure sample with an initial velocity of v_m up to the cease of the simulation, then the stress histories of the assigned element on the incident bar can be obtained.
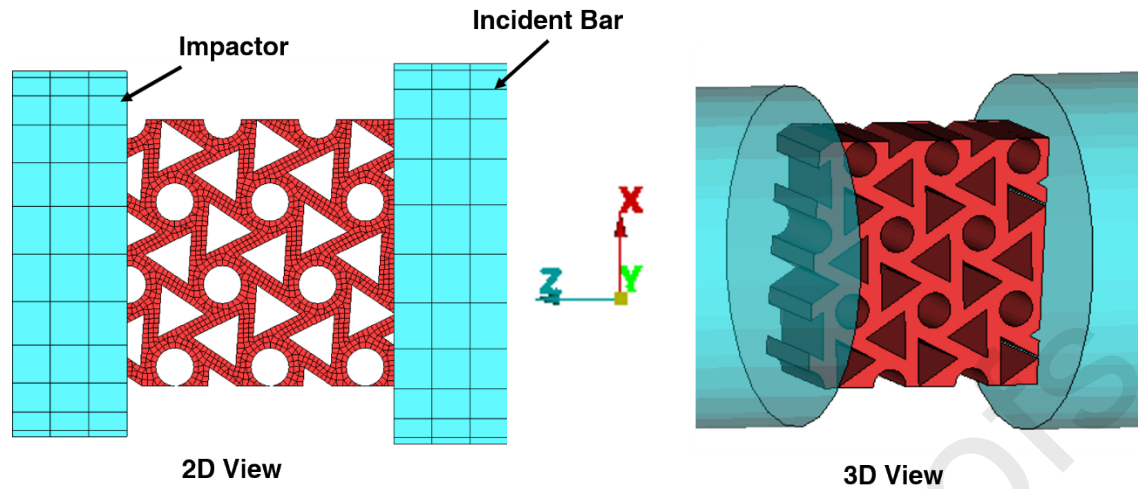
Fig. 7. Schematic diagram of FE model of chiral structure for DI-HPB tests.

In the initial DI-HPB test, the initial contact velocity between the projectile and the chiral structure was 2.36 m/s. The comparison of stress history between the numerical simulation and the experimental test is shown in Fig. 8a. It can be seen that the results from these two methods are very close. The relatively large difference at the initial yield stress at the time of about 0.16 ms may be caused by the initial unstable contact duration from the experimental test. Then, increase the initial velocity of the projectile to the magnitude of 8.43 m/s, Fig. 8b still shows a good agreement between the numerical simulated and experimental recorded stress histories. From the comparison between experimental and simulated results, it can be concluded that the control parameters employed in the creation of the present FE model is correct. The ABAQUS/Explicit model used in the present study has sufficient capability to predict the impact response of the chiral structures.
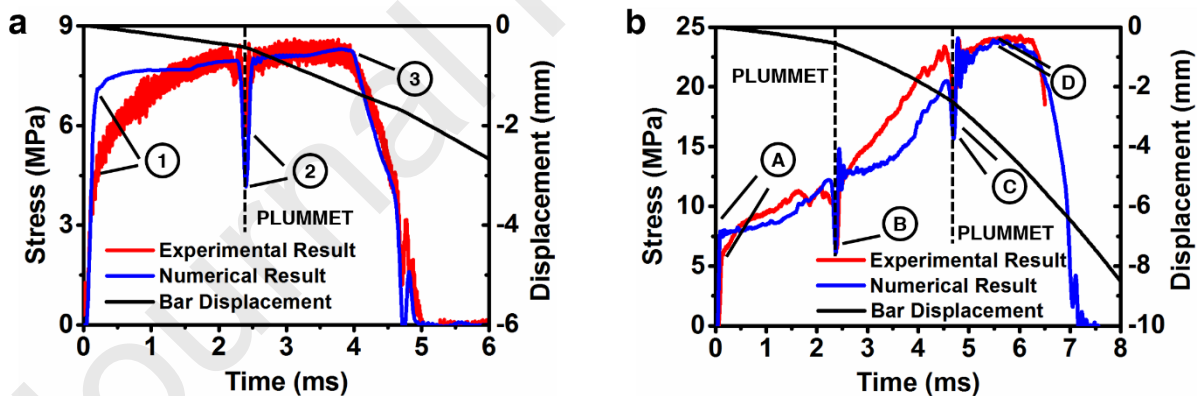

Fig. 8. Comparison of stress histories between numerical simulation and experimental test. a) Initial impact velocity of 2.36 m/s for projectile. b) Initial impact velocity of 8.43 m/s for projectile.

4. Results and discussion

4.1. Plastic evolution and energy absorption of chiral structure in dynamic test

Fig. 9a shows the in-plane deformation process of the specimen in DI-HPB test under the impact speed of 2.36 m/s. The strain evolution was presented by the photographic recordings characterised by DIC technique. This plastic evolution of chiral structure was also captured by FE simulations, as shown in Fig. 9b. The three major marked time points respectively representing the initial peak stress (mark ①), plummet stress (mark ②) and ultimate stress (mark ③) in Fig. 8a were chosen to keep track of the failure status. It can be seen from both

the experimental and simulated results that the plastic strain initiates from the ligaments along the impact direction. Then the plastic strain was further developed and formed a fully plastic zone at some ligaments. As the insufficient kinetic energy of the projectile at current speed, the ultimate crushing strain was about 6.8%. As for the impact speed of 8.43 m/s, the similar plastic evolution characteristics were observed in Fig. 10 corresponding to the marked time points at mark Ⓐ, mark Ⓑ, mark Ⓒ and mark Ⓓ on Fig. 8b. However, the obvious crushing failure of the nodes was observed due to the large impact energy. And the eventual crushing strain of the specimen reached about 45%. It should be noted that it failed to calculate the strain contour using DIC method under the high-speed impact due to the overlap speckles. Meanwhile, the obvious negative Poisson's ratio behaviours in the present DI-HPB impact tests were unexpected as the high relative density and small dimension of the chiral structure.

It is noticed from the stress histories at v_m = 2.36 m/s that they experience a plummet before the stress decrease. The similar phenomenon has also been observed at the impact speed of v_m = 8.43 m/s. However, the stress histories include two unloading/loading processes. This can be explained by the fully plastic deformation at the ligaments. Due to the increase of stress, the displacement of incident bar increased more rapidly along Z-direction with the forming of a fully plastic zone at the plummet, as shown in Fig. 8.
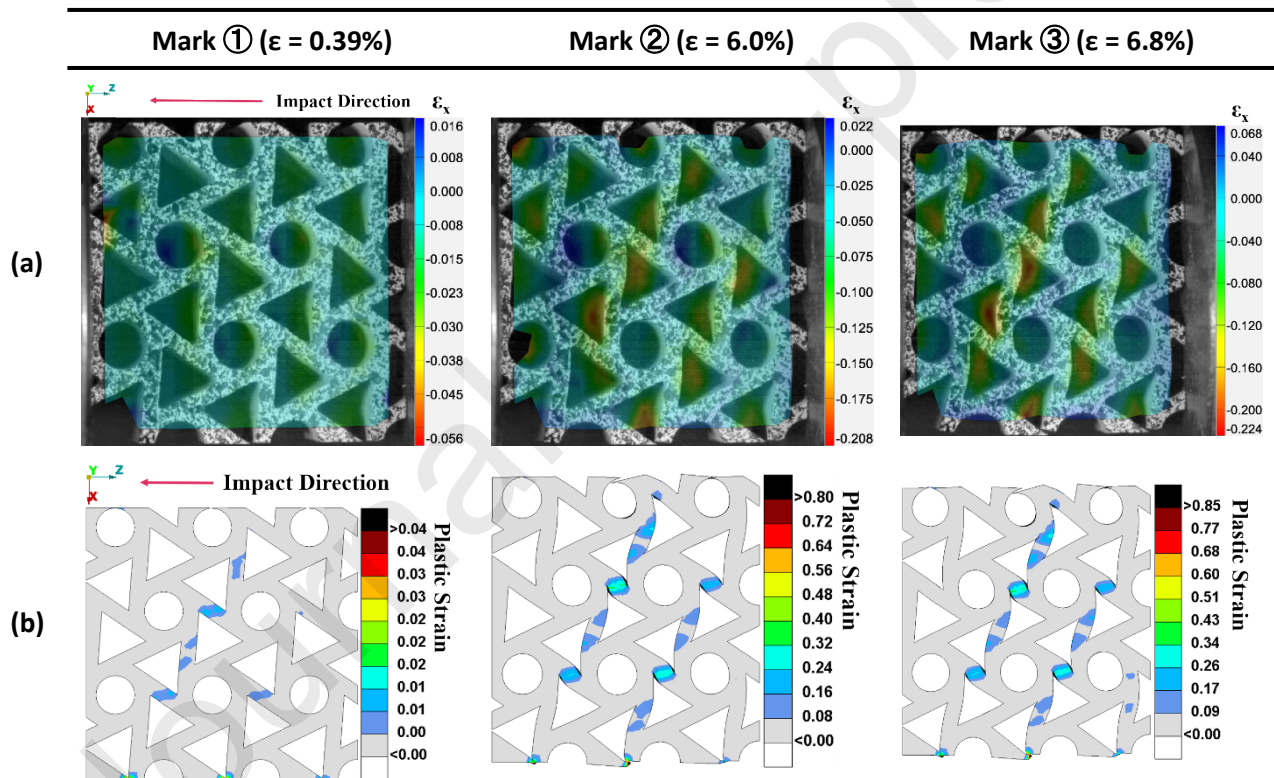

Fig. 9. Deformation process of chiral structure under initial impact speed of 2.56 m/s in DI-HPB tests. a) (Top) Experimental strain contour plot using DIC method. b) (Bottom) Analysis results (plastic strain) by numerical simulations, and corresponding to marked time point in Fig. 6.

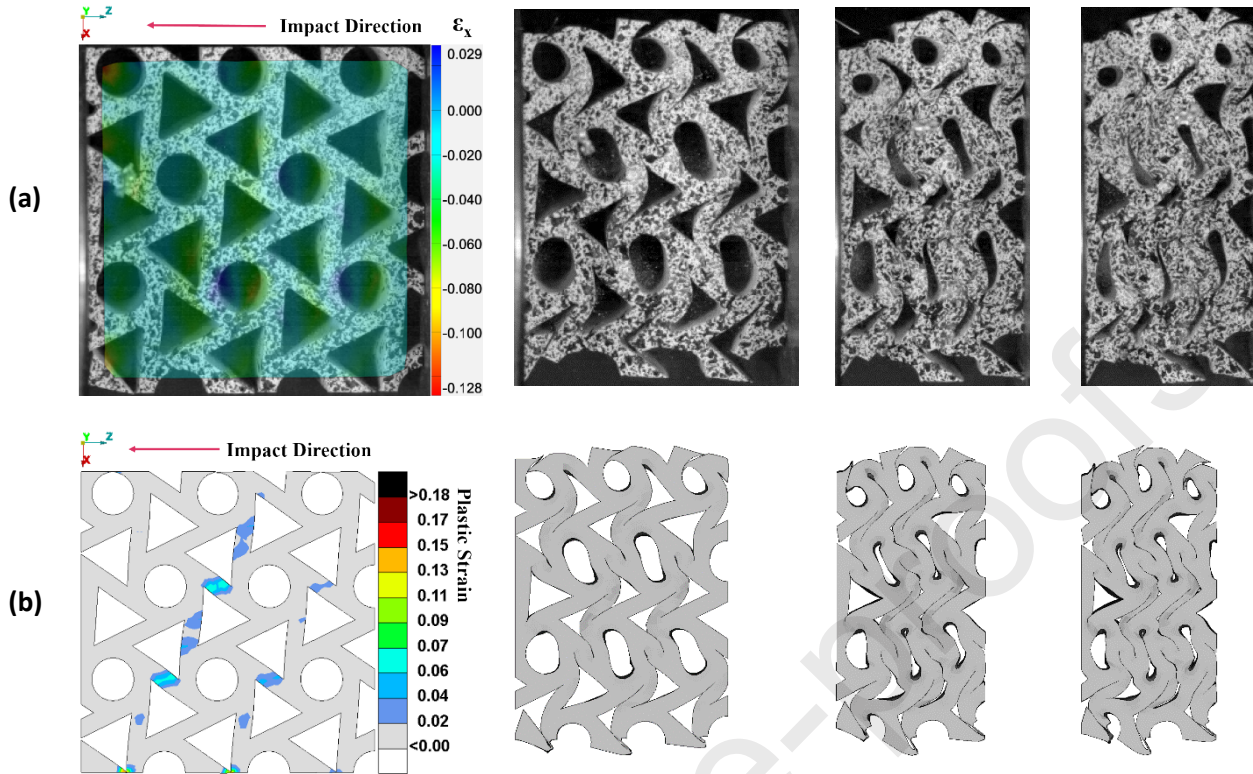| Mark Ⓐ	Mark Ⓑ	Mark Ⓒ	Mark Ⓓ
(ε = 1.3%)	(ε = 25.2%)	(ε = 41.5%)	(ε = 45%)

Fig. 10. Deformation process of chiral structure under initial impact speed of 8.43 m/s in DI-HPB test. a) (Top) Experimental results (strain contour) recorded by a high-speed camera. b) (Bottom) Analysis results (plastic strain) by numerical simulations, and corresponding to marked time point in Fig. 6.

Fig. 11 plots the stress histories of the incident bar in the absence of the samples corresponding to the impact speed of 2.36 m/s and 8.43 m/s, respectively. Compared to the stress histories in Fig. 8, the participation of the chiral lattice structures can significantly attenuate the stress levels developed along the incident bar.
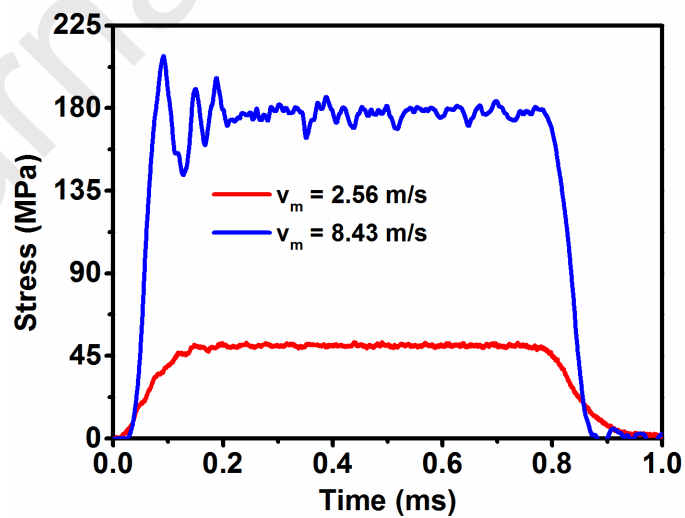

Fig. 11. Experimental stress histories of incident bar in absence of chiral structure.

4.2. Failure mechanism

As a matter of fact, the chiral auxetic structures in the above experimental tests just indicatively represents the dynamic compression behaviour because of the finite number of unit cells along the width and height direction of the specimen. In this section, the failure mechanism of the chiral structures has been investigated by the FE simulations.

Initially, the chiral structure with a wall thickness of $t_l = t_n = 1mm$ was loaded by the rigid wall, the impact velocities of which varied from 5 m/s to 50 m/s. The present range of velocities was determined referring to a normalised velocity $\overline{V}$ which is defined as $\overline{V} = V / (c_0 \varepsilon_Y)$, where $c_0 = (E / \rho)^{0.5}$ represents the elastic wave speed in the constituent material and $\varepsilon_Y = \sigma_Y / E$ [70]. In the present study, $\overline{V}$ varied between 0.53 and 5.3 considering both low-speed impact ($\overline{V} < 1$) and high-speed impact ($\overline{V} > 1$). Three dominated deformation modes corresponding to impact velocities of 5 m/s, 25 m/s and 50 m/s were observed, as shown in Fig. 12. Although aluminium alloys have no obvious strain rate effect under impact loads, deformation modes of cellular structures are sensitive to impact velocities. As for the chiral structure with a relative density of $\overline{\rho} \approx 0.19$, the shrinkage was initiated from the buckling of ligaments near the distal when subjected to a relatively low-speed impact such as v_m = 5 m/s. Almost all the ligament parts in the vicinity of the joints entered the plastic deformation region at the crushing strain of ε = 10%. The ligaments winded around the nodes that they attached and caused their rotational motion. As the compression strain reached to 50%, almost all the ligaments buckled, and each space formed by the three adjacent ligaments was squeezed to maximise the NPR effect. Afterwards, the compressive deformation of nodes dominated the crushing processes. When the impact velocity was increased to 25 m/s, the failure of chiral structure developed from the impact end (proximal end) with the buckling of nodes at the first row and the ligaments attached to nodes. Then, the further compression ushered the lateral shrinkage of the chiral structure from the proximal end to the distal end, which was induced by the rolling of ligaments around the nodes. Similarly, the shrinkage process ceased when the deformation mode of chiral structure transferred to pure nodes crushing deformation. Continually increasing the impact speed to 50 m/s, the crushing processes obviously involved both ligaments failure and nodes failure at the very beginning of the impact near the proximal end. The localised impact deformation suppressed part of the complete rolling process of the ligaments around the nodes especially these close to the impact end. In contrast to the global plastic failure mechanism of the chiral structures subjected to low-speed impact loading, the local plastic failure dominates the entire crushing deformation.

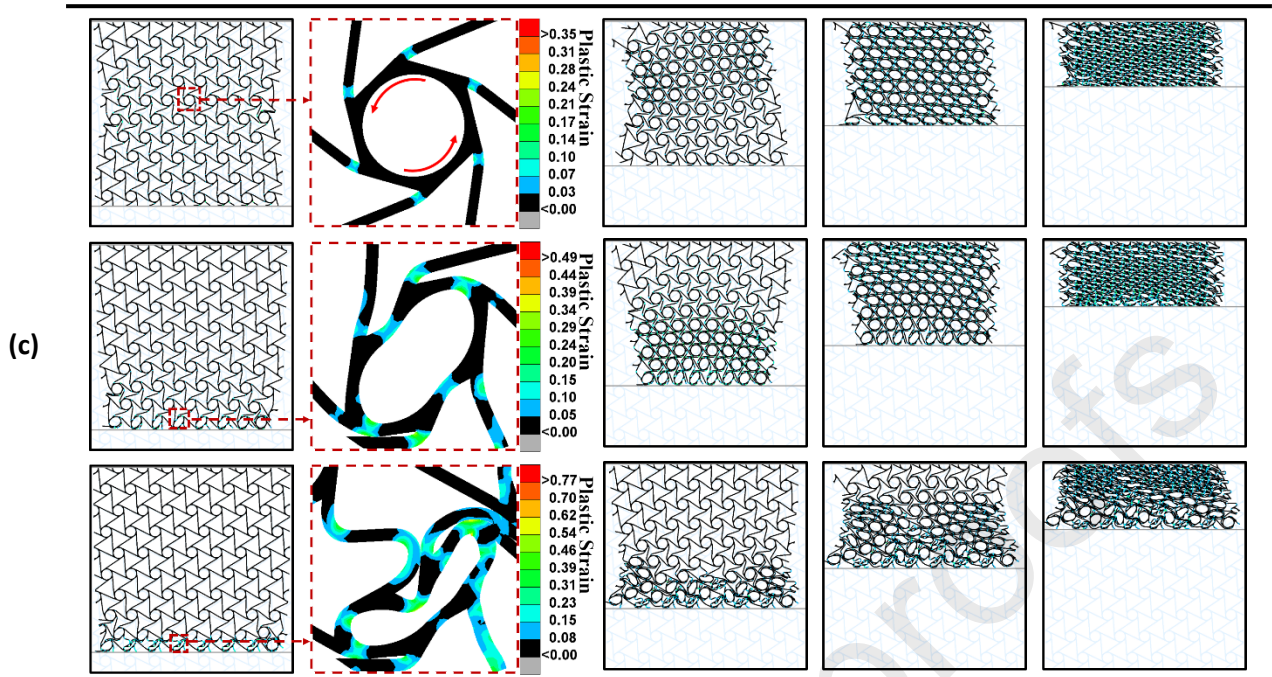| ε = 10%	Initial Failure	ε = 30%	ε = 50%	ε = 70%

(a)

(b)

Fig. 12. Crushing deformation and initial failure mode with plastic strain contour plot of chiral structure corresponding to impact speed of 5 m/s, 25 m/s and 50 m/s.

Fig. 13 plots the impact force of the chiral structures under a certain crushing velocity as a function of strain. It can be seen that the crushing forces generated by the motion of the rigid wall against the chiral structure tend to present a positive relationship to the impact velocities. In the general view of the force-strain curve at the low-speed impact (v_m = 5 m/s), the initial peak formed followed by a large plateau stress region, then the stress value increases continually due to the structural first stage of the densification from the sufficient participation of nodes in the crushing processes. Increasing the impact speed to 25 m/s slightly distorts the crushing plateau, which is caused by the partial crushing failure of nodes. The multi-peak stress is observed from the force-strain curve at the impact speed of 50 m/s since the sufficient axial compression deformation of ligaments participated in the crushing processes.

In the current case, the limiting strain of first stage densification of the chiral structures is dependent on the impact velocities. The increase of the impact velocities results in the late densification of the chiral structures. The indication of the first stage densification for the chiral structures is deemed to be the completely node-dominated crushing deformation.
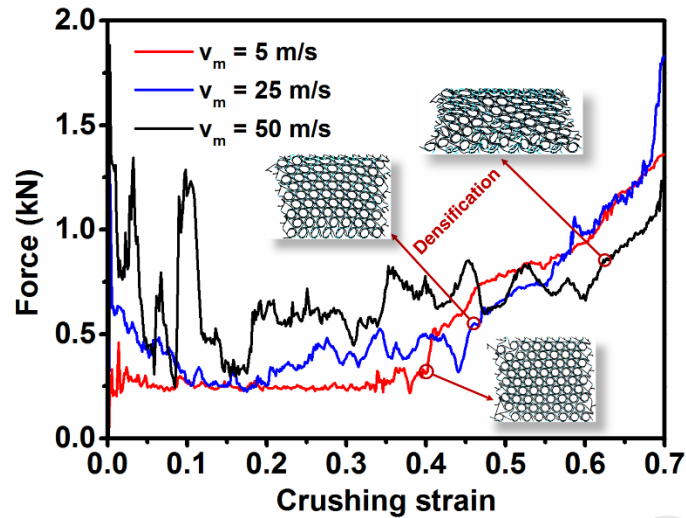
Fig. 13. Force-strain curves and densification of chiral structures corresponding to impact velocities varied from 5 m/s to 50 m/s.

4.3. Parametric studies

In this section, five crucial impact parameters used for the evaluation of the impact performance of the present chiral structures have been defined: total plastic energy absorption (TEA), specific plastic energy absorption (SEA), crushing force efficiency (CFE), cushion factor (CF) and Poisson's ratio (v). Based on these five parameters, the effect of the relevant density, the unit cell geometry and the initial impact energy has be identified numerically. To avoid counting the output in the ultimate densification stage, all the parameters were calculated up to the strain of 0.6.

The TEA here is the output of the total strain energy dissipated by the plastic deformation of chiral structures in the crushing processes. The SEA is defined as the plastic energy dissipated per unit mass of the crushed sample, namely $SEA = TEA / m$. The parameter of SEA is important to determine the appropriate design of specimen with the lightweight objective and the higher SEA is preferred. The CFE represents the ratio of the average impact force F_{av} to the maximum impact force F_{max} in the total impact processes and is expressed as $CFE = F_{av} / F_{max}$. The F_{av} is obtained by dividing the total absorbed energy (the area under the load-displacement curve) by the crushing displacement. The F_{max} is either the value of initial peak force or the ultimate force at the crushing strain of 0.6. The CFE is an effective measure for the uniformity of crushing force and higher CFE is preferred. The cushion factor is calculated as $CF = F_{max} / TEA$, which is useful to balance the structural design between structural crashworthiness and safety of protected equipment. The lower CF is preferred. The Poisson's ratio (v) is given as $v = -\varepsilon_{trans}/\varepsilon_{axial}$. The transverse strain (ε_{trans}) and the axial strain (ε_{axial}) are defined as the ratio of change in width and height direction of the chiral specimen due to the crushing deformation and are measured at the ultimate strain before the densification at the second stage (nodes-dominated crushing densification). As the irregular transverse shrinkage deformation, the minimum absolute value of ε_{trans} is considered in the present study.

4.3.1. Effect of relative density

In order to evaluate the effect of relative density on the impact parameters of chiral structures, the numerical simulation of chiral structure under impact load was conducted considering different values of the structural relative densities varying from 0.19 to 0.39. The same FE model described in Section 4.2 was used for the present study. The various values of structural relative densities were obtained by synchronously changing the thickness of both the ligaments and nodes between 1 mm and 2 mm with an increment of 0.25 mm while

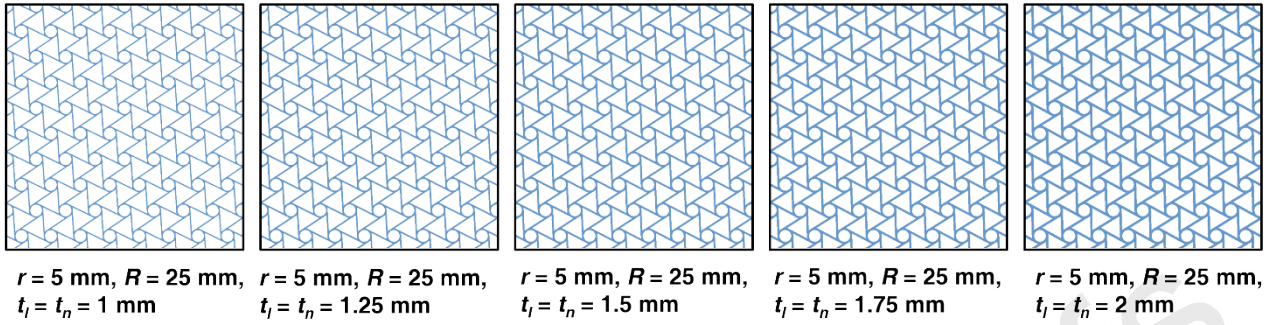the topology parameter r/R was kept constant, as shown in Fig. 14.

$r = 5$ mm, $R = 25$ mm, $t_l = t_n = 1$ mm $r = 5$ mm, $R = 25$ mm, $t_l = t_n = 1.25$ mm $r = 5$ mm, $R = 25$ mm, $t_l = t_n = 1.5$ mm $r = 5$ mm, $R = 25$ mm, $t_l = t_n = 1.75$ mm $r = 5$ mm, $R = 25$ mm, $t_l = t_n = 2$ mm

Fig. 14. Geometry of chiral structures corresponding to increasing wall thickness from $t_l=t_n=1$ mm to $t_l=t_n=2$ mm (left to right) while keeping topology parameter r/R constant.

Fig. 15 presents the variation of SEA with relative density. Meanwhile, for the SEA under each relative density, three crushing velocities of 5 m/s, 25 m/s and 50 m/s were considered in this study. The crushing velocities keep always constant during the entire crushing processes. It can be seen that the SEA increases significantly by varying the relative density from 0.19 to 0.39. For the same relative density, the relatively slight increase in SEA is also observed as the crushing velocity increases.

Figs. 16-18 plots the CFE, CF and Poisson's ratio (ν) of chiral structures under different relative densities, and the effect of crushing velocity is also presented. It is observed that the impact parameters are comparatively independent on structural relative density at the crushing velocities of 5 m/s and 25 m/s. When it is subjected to the crushing velocity of $v_m = 50$ m/s, the chiral structure with larger relative density shows the superiority over that with lower relative density on CFE and CF. The Poisson's ratio (ν) increases dramatically as changing the crushing velocity from 25 m/s to 50 m/s but still keeps a negative value. This can be explained by observing the densification deformation of chiral structures in Fig. 19. When the value of impact velocity is relatively low (e.g. $v_m = 5$ m/s), the ligaments bending failure dominates the entire lateral shrinkage deformation and contributes to exhibit a negative Poisson's ratio behaviour for all the chiral structures regardless of the values of relative density. However, when it comes to high-speed impact (e.g. $v_m = 50$ m/s), a sufficient number of ligaments and nodes bulk simultaneously due to the dynamic effect. Since the high strength of nodes and low porosity, the chiral structures having large value of relative density are still capable to allow more ligaments winding around the nodes compared to that having smaller value of relative density. It is apparent that the increase of structural relative density causes the early densification for both low-speed and high-speed impact.

Table 2 presents energy absorption rate during first stage of densification for different values of relative density of chiral structure. It can be seen from the table that percentage of plastic energy absorption in the first stage of densification (ligaments-dominated crushing deformation) generally increases with impact velocity and decreases with relative density. When subjected to the impact velocity of $v_m = 5$ m/s and $v_m = 25$ m/s, the chiral structure with small value of relative density shows better flexibility in structural design. However, the converse is noted when the impact velocity increases to $v_m = 50$ m/s.
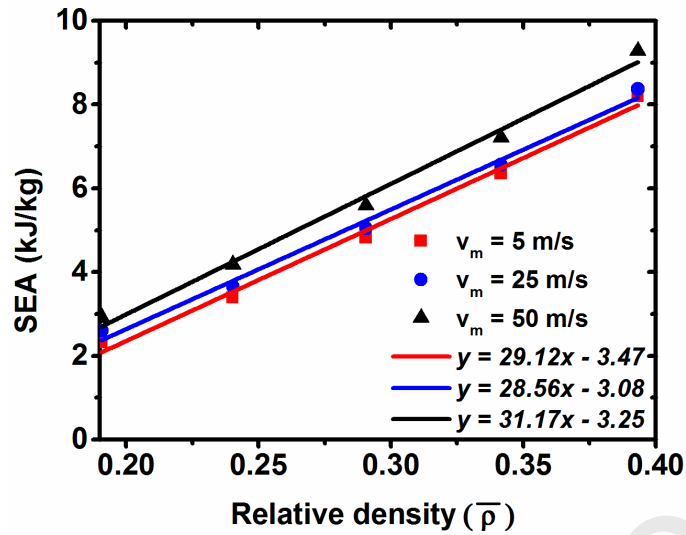
Fig. 15. SEA of chiral structures corresponding to different relative densities.
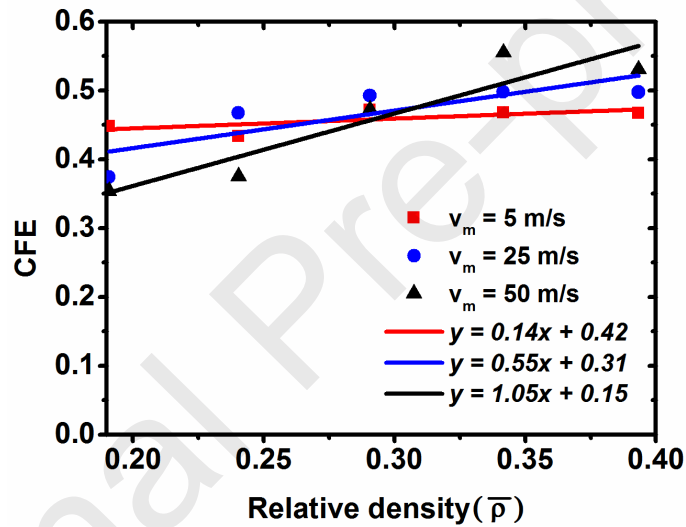

Fig. 16. CFE of chiral structures corresponding to different relative densities.
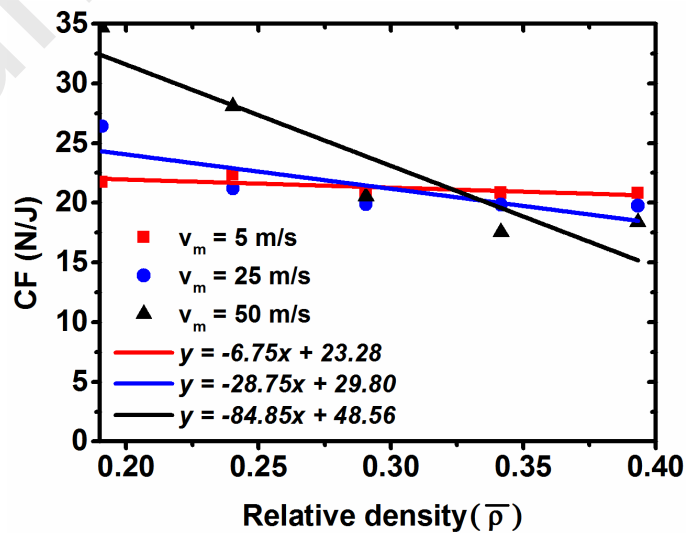
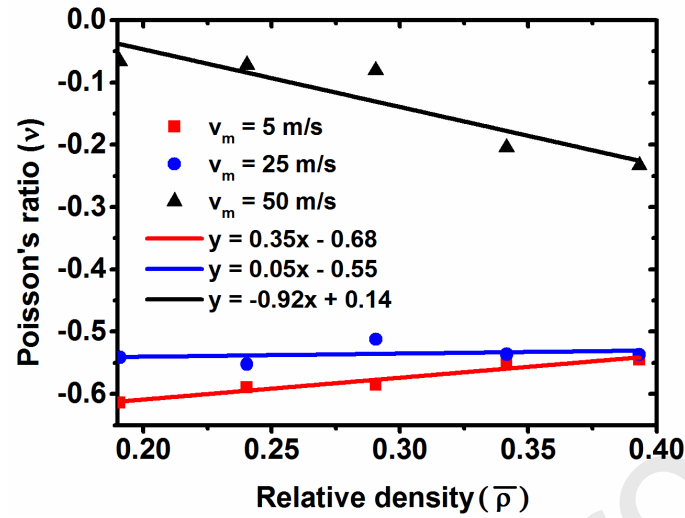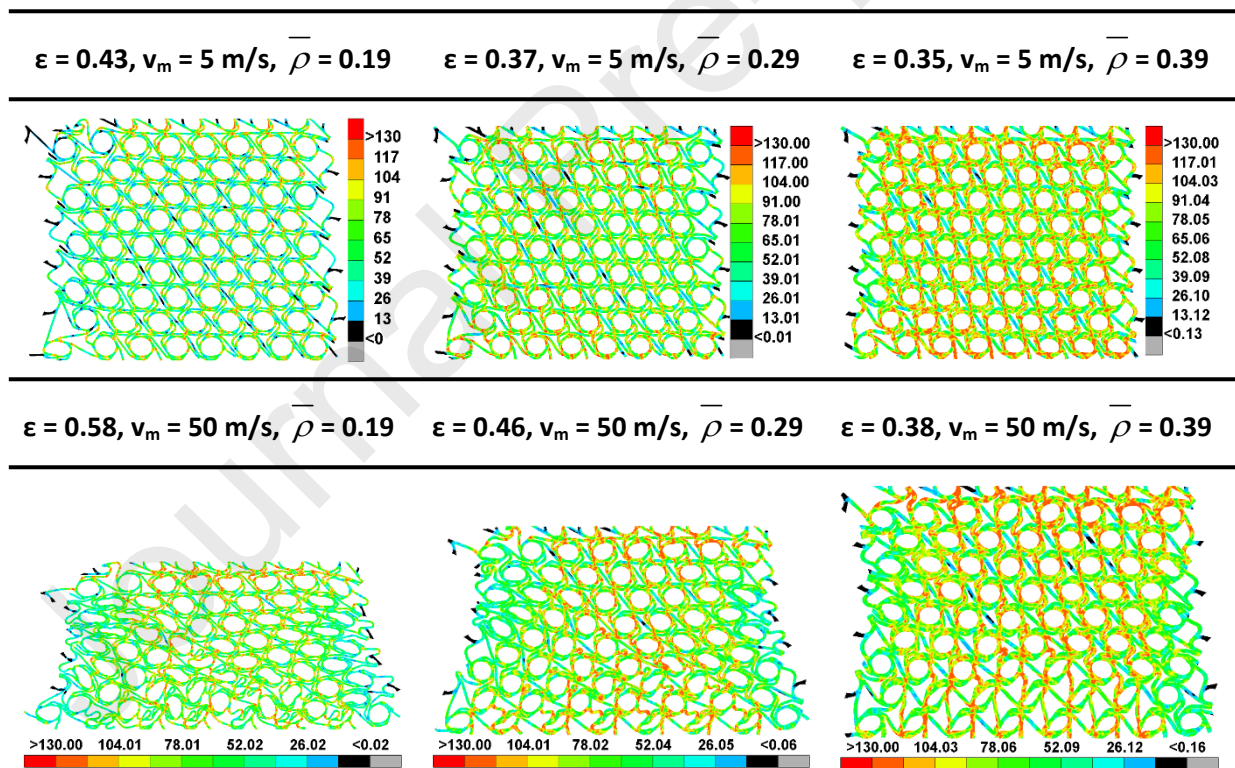**Fig. 17.** CF of chiral structures corresponding to different relative densities.

Fig. 18. Poisson's ratio (v) of chiral structures corresponding to different relative densities.

Fig. 19. Low-speed (v_m = 5 m/s) and high speed (v_m = 50 m/s) impact deformation at first densification (about to nodes-dominated crushing process) for chiral structures having different values of relative density.

Table 2 Energy absorption rate during first stage of densification for different values of relative density of chiral structure.

	$\bar{\rho}$ = 0.19	$\bar{\rho}$ = 0.24	$\bar{\rho}$ = 0.29	$\bar{\rho}$ = 0.34	$\bar{\rho}$ = 0.39
v_m = 5 m/s	44.2%	38.8%	33.8%	31.2%	30.3%
v_m = 25 m/s	52.5%	45.2%	37.8%	34.1%	29.6%
v_m = 50 m/s	91.6%	70.8%	60.1%	49.6%	41.6%

Note: The value is calculated by ($TEA_{Densification\_1}$/ $TEA_{60\%Crushing}$)%.

4.3.2. Effect of topology parameter r/R

When varying the ratio of the topology parameter r/R, it will exhibit possible topologies ranging from a hexagonal arrangement of rings ($r/R \rightarrow 1$) to the classic triangular lattice （$r/R \rightarrow 0$）[56]. In order to investigate the effect of the present topology parameter r/R on the impact parameters, the parametric study was conducted by tuning the ratio of r/R between 1/5 to 1/25 (e.g., see Fig. 20). In the present study, the parameter R was always kept constant of 25 mm, but the parameter r ranged between 1 mm and 5 mm. Meanwhile, the total mass of the chiral structures corresponding to different ratio of r/R was kept constant by changing the wall thickness between 1 mm and 1.217 mm.
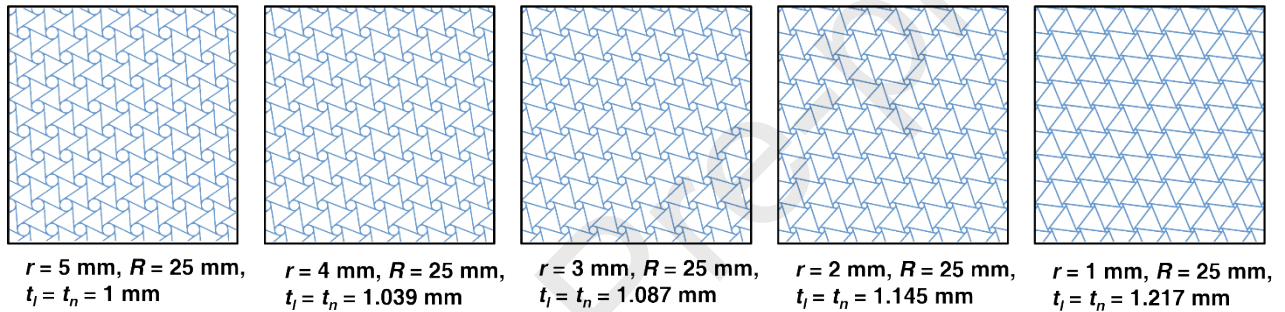

r = 5 mm, R = 25 mm, $t_l = t_n$ = 1 mm   r = 4 mm, R = 25 mm, $t_l = t_n$ = 1.039 mm   r = 3 mm, R = 25 mm, $t_l = t_n$ = 1.087 mm   r = 2 mm, R = 25 mm, $t_l = t_n$ = 1.145 mm   r = 1 mm, R = 25 mm, $t_l = t_n$ = 1.217 mm

Fig. 20. Geometry of chiral structures corresponding to decreasing r/R from r/R=1/5 to r/R=1/25 (left to right) while keeping the total mass constant.

Figs. 21-24 show respectively the TEA, CFE, CF and Poisson's ratio (v) curves of the chiral structures corresponding to different ratio of r/R while the total mass keeps constant. It is observed that the small r/R tends to absorb more plastic energy for all the crushing velocities. However, the TEA changes slightly with r/R if the crushing velocity is small enough. When the r/R varying between 0.04 and 0.2, the small r/R has lower CFE, larger CF but larger TEA under the crushing velocities of v_m = 25 m/s and v_m = 50 m/s. Nevertheless, although low crushing velocity (e.g., v_m = 5 m/s) results in the smaller plastic energy dissipation, desired impact performance such as high CFE and low CF can be achieved. When subjected to the crushing velocities of v_m = 5 m/s and v_m = 25 m/s, the topology parameter r/R can significantly influence structural Poisson's ratio which decreases with the increase of r/R. The slight variation of the Poisson's ratio with the r/R is observed when continually increasing the crushing velocity to be v_m = 50 m/s. The chiral structure exhibits an average Poisson's ratio of v ≈ -0.6. The negative Poisson's effect is not observed as the r/R is sufficiently small (e.g., r/R = 0.04). This is clearly explained as the densification deformation shown in Fig. 25. With the decreasing value of nodes radius, the ligaments cannot make a full twist around the attached node, which results in the ligaments stacking up row by row disorderly.

Table 3 presents energy absorption rate during first stage of densification for different values of r/R of chiral structure. It can be seen from the table that the percentage of plastic energy absorption in the first stage of densification (ligaments-dominated crushing deformation) decreases with r/R and increases with impact velocity. No obvious second stage densification of chiral structure will be observed if r/R is sufficiently small

such as *r/R* = 0.04 and *r/R* = 0.08. Generally, the chiral structure with large value of *r/R* shows better flexibility in structural design.
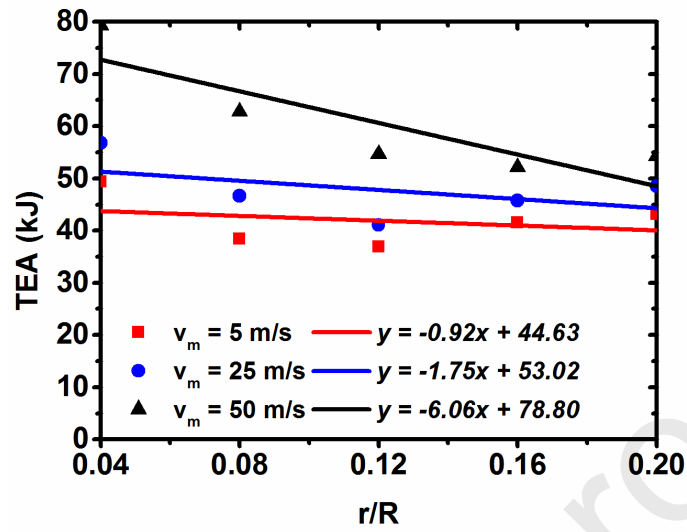

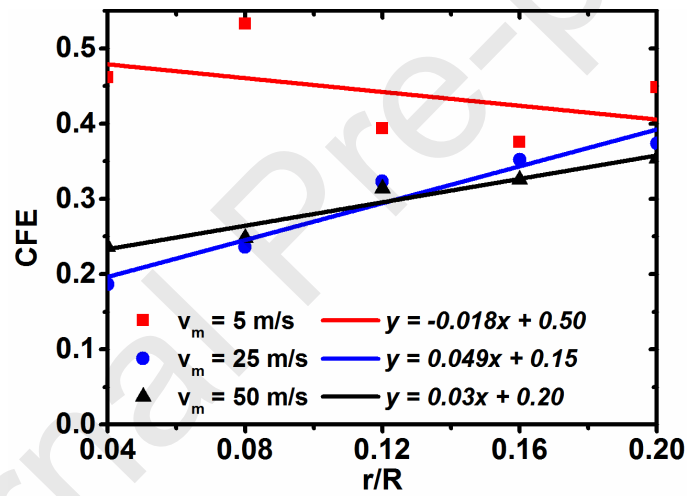**Fig. 21.** TEA of chiral structures corresponding to different r/R.

Fig. 22. CFE of chiral structures corresponding to different r/R.
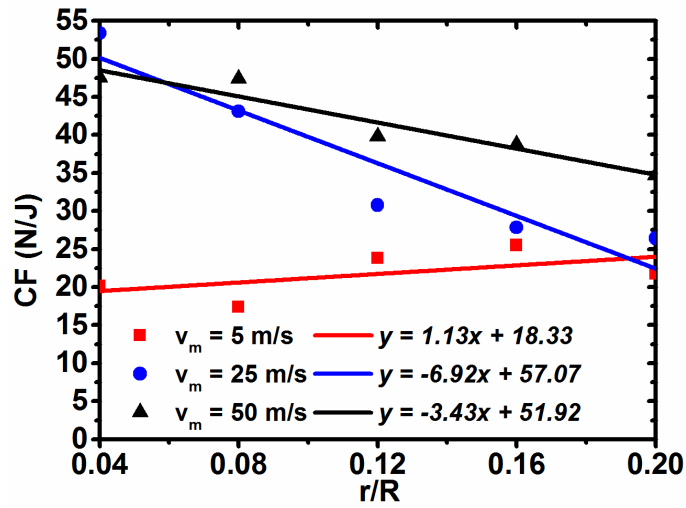
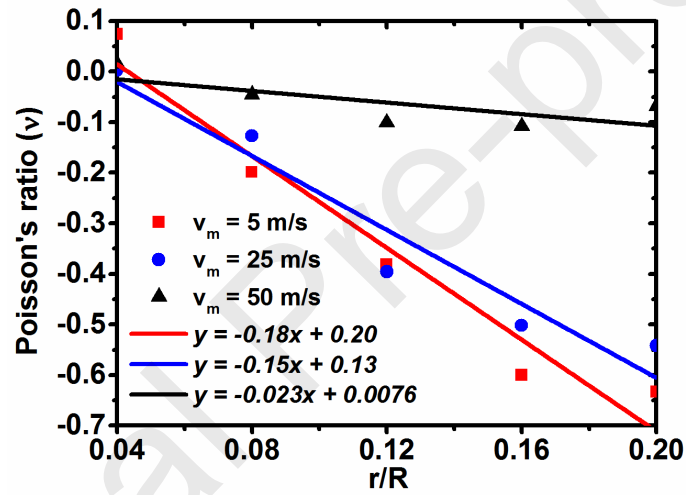**Fig. 23.** CF of chiral structures corresponding to different r/R.

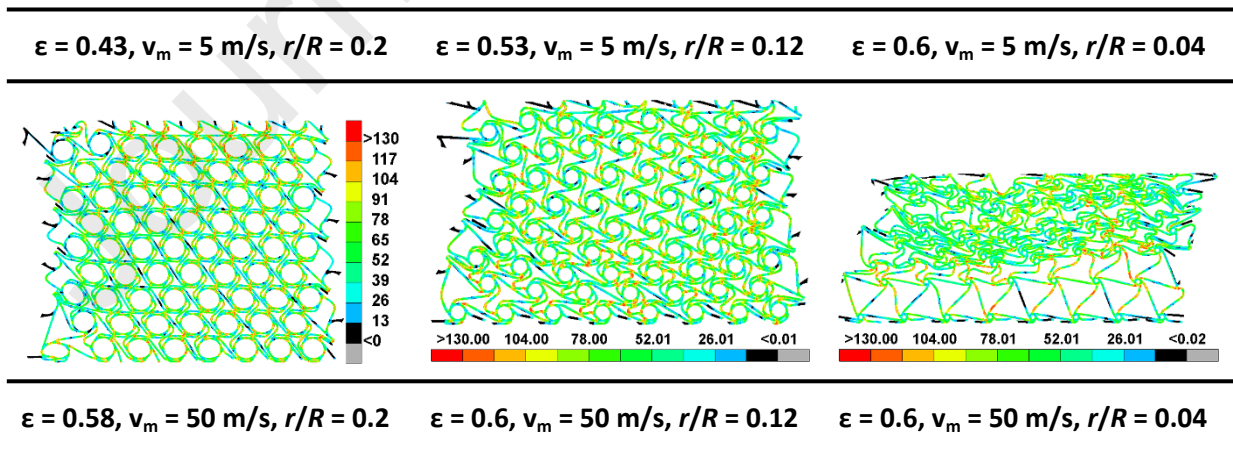**Fig. 24.** Poisson's ratio (v) of chiral structures corresponding to different r/R.

ε = 0.43, v_m = 5 m/s, r/R = 0.2	ε = 0.53, v_m = 5 m/s, r/R = 0.12	ε = 0.6, v_m = 5 m/s, r/R = 0.04

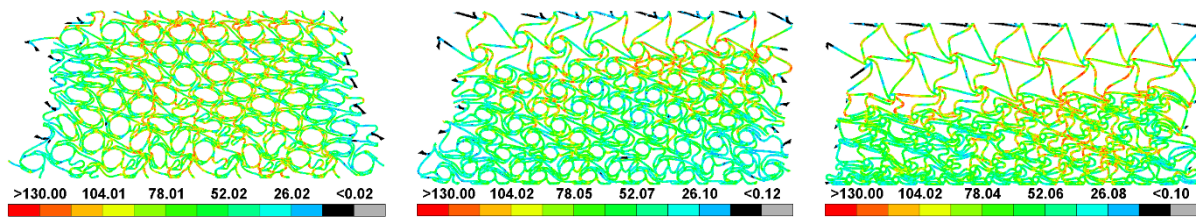| ε = 0.58, v_m = 50 m/s, r/R = 0.2	ε = 0.6, v_m = 50 m/s, r/R = 0.12	ε = 0.6, v_m = 50 m/s, r/R = 0.04

Fig. 25. Low-speed (vm = 5 m/s) and high speed (vm = 50 m/s) impact deformation at the first densification (about to nodes-dominated crushing process) for chiral structures having different values of r/R.

Table 3 Energy absorption rate during first stage of densification for different values of *r/R* of chiral structure.

	r/R = 0.04	*r/R* = 0.08	*r/R* = 0.12	*r/R* = 0.16	*r/R* = 0.20
v_m = 5 m/s	100%	100%	80.3%	52.1%	44.2%
v_m = 25 m/s	100%	100%	91.2%	64.1%	52.5%
v_m = 50 m/s	100%	100%	100%	99.7%	91.6%

Note: The value is calculated by ($TEA_{Densification\_1}$/ $TEA_{60\%Crushing}$)%.

4.3.3. Effect of initial impact energy

In order to investigate the inertia effect on the impact performance of chiral structures, the same ABAQUS/Explicit simulation model as employed in section 4.2 was used in the present study, but the constant impact energy was replaced by different values of initial impact velocity and mass.

Specifically, the effect of impact velocity on impact behaviour of chiral structures was explored for a constant impact mass of 0.5 kg while the value of initial impact velocity changing between v_i = 5 m/s and v_i = 11 m/s. Fig. 26 presents the impact force-displacement curves for different initial impact velocities ranging from v_i = 5 m/s to v_i = 11 m/s. It can be seen that the increase of initial impact velocities causes the growing crushing displacement as the growth of initial kinetic energy. Fig. 27 shows the forces-time curves and ultimate deformations of chiral structures under different impact velocities. Since the participation of first stage densification, the impact at v_i = 11 m/s terminates prior to that at v_i = 9 m/s and causes the rapid increase of impact force.

Fig. 28 plots the impact force-displacement curves for different initial values of impact mass ranging from m = 0.5 kg to m = 2.42 kg. Similarly, the crushing distance increases with the increase of initial impact mass value. Fig. 29 plots the force-time curves for different values of impact mass. Nevertheless, although the impactors (e.g. v_i = 7 m/s, m = 0.98 kg or v_i = 9 m/s, m = 1.62 kg or v_i = 11 m/s, m = 2.42 kg) possesses the same initial impact energy, the impact terminates at different times and higher initial impact velocity tends to dissipate the energy more rapidly. Instead, the crushing displacement is independent of initial impact velocity and impact mass and is determined by the initial impact energy. It is also noted that the impact curves for different values of impact mass present higher convergence up to the rebounding displacement than that for different initial impact velocities.
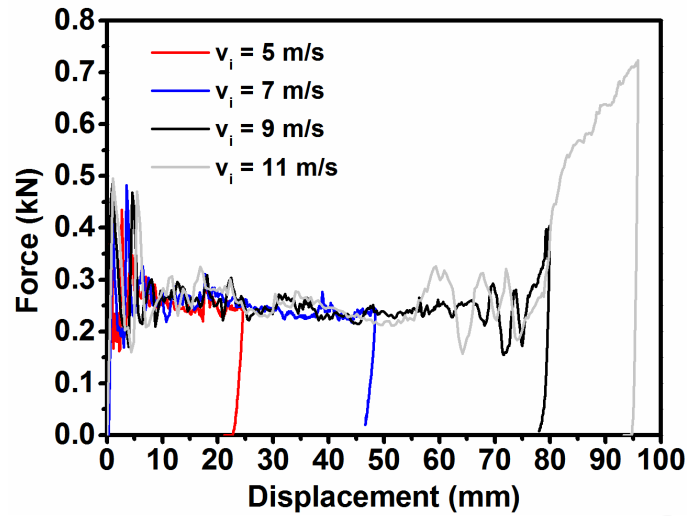
Fig. 26. Force-displacement curves under different impact velocities while impact mass is 0.5 kg.
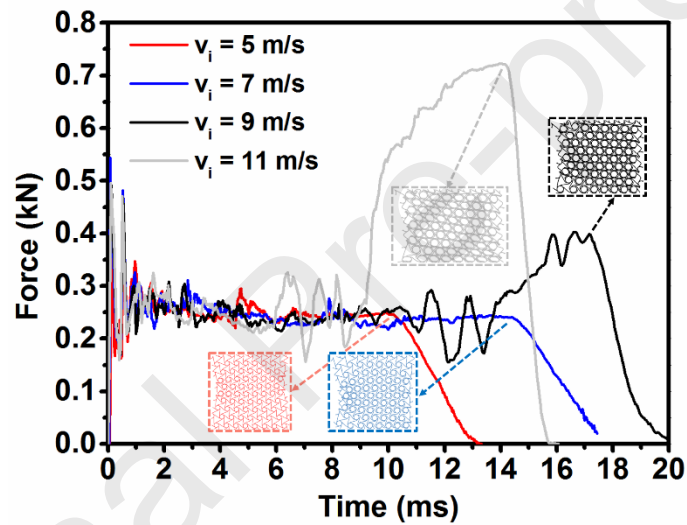

Fig. 27. Force-time curves and ultimate deformations under different impact velocities while impact mass is 0.5 kg.
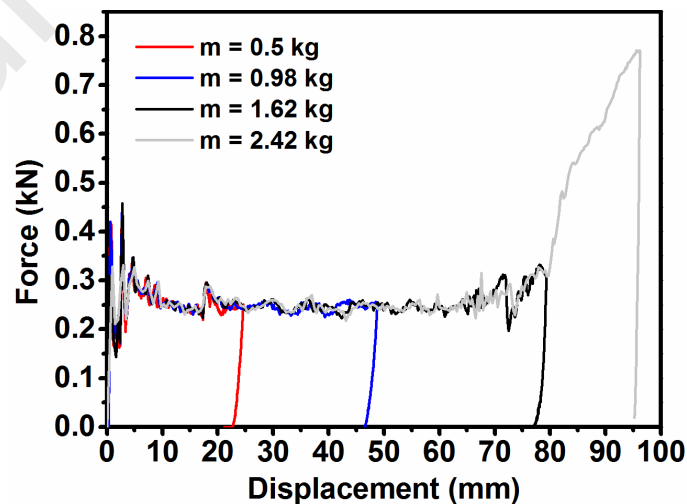

Fig. 28. Force-displacement curves for different values of impact mass while impact velocity is 5 m/s.
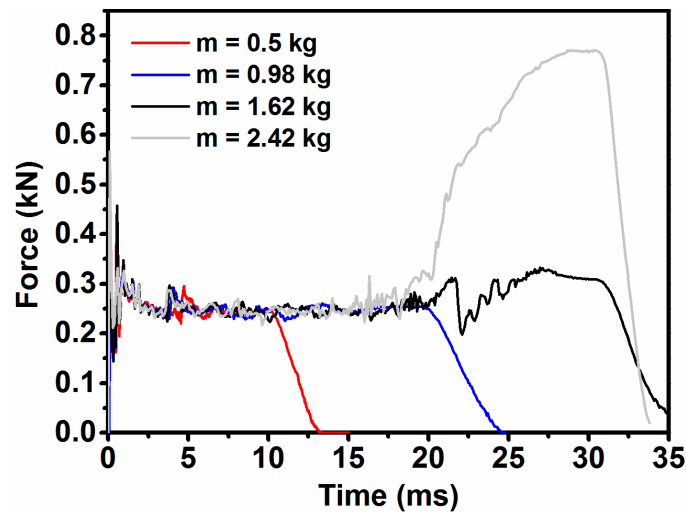
Fig. 29. Force-time curves for different values of impact mass while impact velocity is 5 m/s.

4.4. Comparison with other cellular structures

In order to compare the plastic energy dissipation capacity of the chiral structure in this study with other cellular structures, the dissipated plastic energy was normalised as $\bar{U}_P = U_P / \sigma_{YC} V_{ol}$. In this expression, U_P is total plastic energy dissipation, V_{ol} is volume of structure, $\sigma_{YC} = 0.5\bar{\rho}^2 \sigma_Y$ is effective yield strength. The results on normalised plastic energy dissipation, in combination with that of hexagonal honeycomb [66], re-entrant structure [26] and arrowhead honeycomb [5] in the previous study by other researchers, are presented in Fig. 30. With the increase of crushing velocity, the plastic energy dissipation capacity increases significantly. It is noted that the current chiral structure has lower inertial effect than other cellular structures. Chiral structure presents better plastic energy dissipation capacity than re-entrant structures at relatively low crushing velocity, especially at 70% crushing strain. Because the second densification stage of chiral structure plays a more important role in energy absorption than the first densification stage.
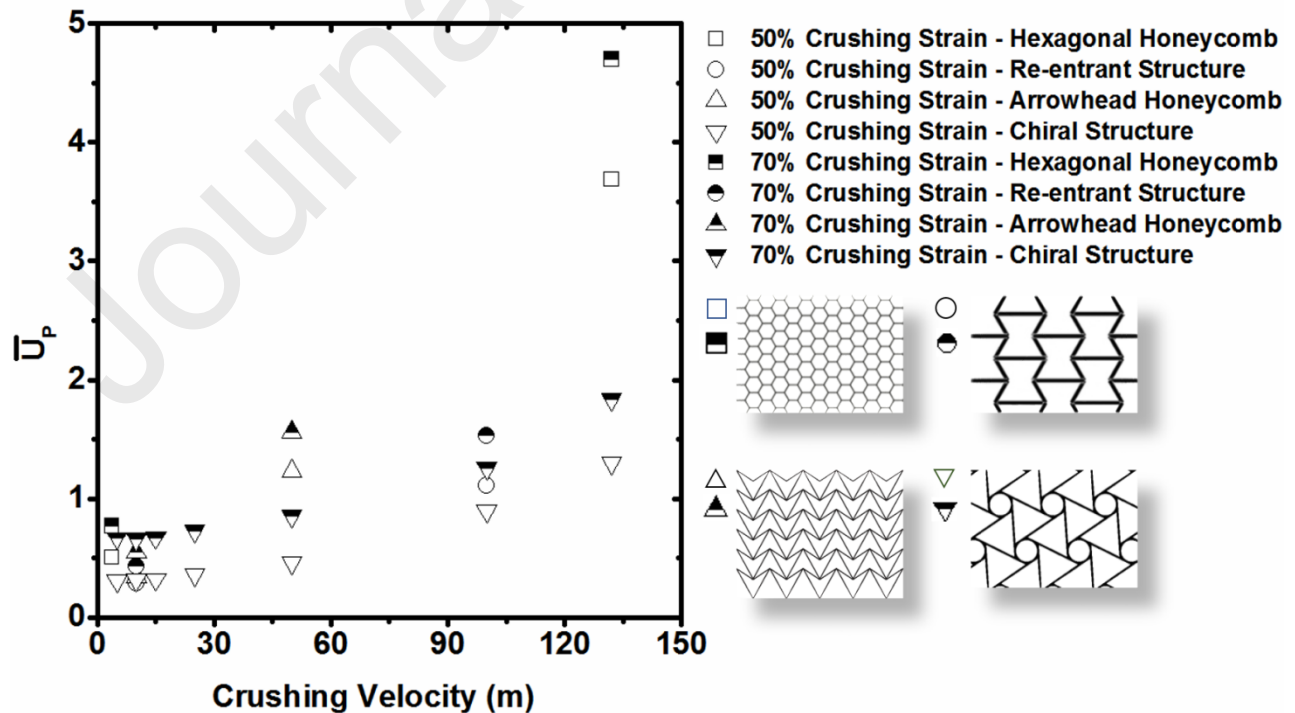
Fig. 30. Normalised plastic energy dissipation of different cellular structures under compressive loading. The results for hexagonal honeycomb, re-entrant structure and arrowhead honeycomb are obtained from the study by other researchers[5, 26, 66].

5. Conclusions

The in-plane compressive behaviour of chiral structures has been investigated by both experimental tests and numerical simulations. The explicit nonlinear finite element models were validated by comparing the impact response in terms of impact force history with the experimental results. It is observed that there are good agreements between numerical and experimental results. Afterwards, the plastic evolution, energy absorption and failure mechanism of chiral structures have been discussed in terms of both DI-HPB test and numerical simulation. Moreover, the parametric study has been conducted to investigate the effects of several parameters such as the relative density, topology parameter r/R, initial impact velocity and mass on the in-plane impact performance of chiral structures. From the results of this study, the main conclusions can be drawn as follows:

(1) Chiral structure initiates the crushing deformation by three important failure modes: Ⅰ - ligaments buckling; Ⅱ - combined nodes and ligaments buckling; Ⅲ - crushed nodes and ligaments corresponding to the impact velocity of 5 m/s, 25 m/s and 50 m/s, respectively. The failure mode transformed from global buckling of the structure to the local bucking at the impact end as the increasing impact velocity.

(2) Chiral structure occurs with two densification stages induced by ligaments-dominated crushing and nodes-dominated crushing deformation. Small value of relative density and large value of r/R present better designability of chiral structure. However, chiral structure with large value of relative density is preferred when the impact velocity is sufficiently high such as v_m = 50 m/s.

(3) Increasing the value of structural relative density from 0.19 to 0.39 contributes to a maximum 250% increase in specific energy absorption. When subjected to high-speed impact such as v_m = 25 or 50 m/s, impact performance in terms of crushing force efficiency and cushion factor benefits from the increase of r/R. Although increasing r/R from 0.04 to 0.2 can dramatically decrease Poisson's ratio from 0.07 to -0.63, structural Poisson's ratio is still highly controlled by the crushing velocity.

(4) The impact displacement is mainly influenced by the initial energy but not the impact velocity and mass. The participation of first stage densification causes the rapid increase of impact force, but it significantly reduces the crushing duration time.

(5) In comparison with other auxetic structures, chiral structure subjected to relatively low impact velocity presents better plastic energy dissipation capacity at 70% crushing strain. Meanwhile, the current chiral structure in this paper has lower inertial effect than the other cellular structures in a wide range of impact velocities.

Data availability

The raw and processed data required to reproduce these findings cannot be shared at this time as the data also forms part of an ongoing study.

References

[1]   Papka SD, Kyriakides S. In-plane compressive response and crushing of honeycomb. Journal of the Mechanics and Physics of Solids. 1994;42:1499-1532.

[2]   Cricrì G, Perrella M, Calì C. Honeycomb failure processes under in-plane loading. Composites Part B: Engineering. 2013;45:1079-1090.

[3]   Hönig A, Stronge WJ. In-plane dynamic crushing of honeycomb. Part I: crush band initiation and wave trapping. International Journal of Mechanical Sciences. 2002;44:1665-1696.

[4]   Ruan D, Lu G, Wang B, Yu TX. In-plane dynamic crushing of honeycombs—a finite element study. International Journal of Impact Engineering. 2003;28:161-182.

[5]   Qiao JX, Chen CQ. Impact resistance of uniform and functionally graded auxetic double arrowhead honeycombs. International Journal of Impact Engineering. 2015;83:47-58.

[6]   Foo CC, Chai GB, Seah LK. Mechanical properties of Nomex material and Nomex honeycomb structure. Composite Structures. 2007;80:588-594.

[7]   Liu Y, Zhang XC. The influence of cell micro-topology on the in-plane dynamic crushing of honeycombs. International Journal of Impact Engineering. 2009;36:98-109.

[8]   Qiao J, Chen C. In-plane crushing of a hierarchical honeycomb. International Journal of Solids and Structures. 2016;85-86:57-66.

[9]   Ashab ASM, Ruan D, Lu G, Wong YC. Quasi-static and dynamic experiments of aluminum honeycombs under combined compression-shear loading. Materials & Design. 2016;97:183-194.

[10]   Hou B, Pattofatto S, Li YL, Zhao H. Impact behavior of honeycombs under combined shear-compression. Part II: Analysis. International Journal of Solids and Structures. 2011;48:687-697.

[11]   Tounsi R, Markiewicz E, Haugou G, Chaari F, Zouari B. Dynamic behaviour of honeycombs under mixed shear-compression loading: Experiments and analysis of combined effects of loading angle and cells in-plane orientation. International Journal of Solids and Structures. 2016;80:501-511.

[12]   Liu Q, Fu J, Wang J, Ma J, Chen H, Li Q, et al. Axial and lateral crushing responses of aluminum honeycombs filled with EPP foam. Composites Part B: Engineering. 2017;130:236-247.

[13]   Xu S, Beynon JH, Ruan D, Yu TX. Strength enhancement of aluminium honeycombs caused by entrapped air under dynamic out-of-plane compression. International Journal of Impact Engineering. 2012;47:1-13.

[14] Zhang Y, Lu M, Wang CH, Sun G, Li G. Out-of-plane crashworthiness of bio-inspired self-similar regular hierarchical honeycombs. Composite Structures. 2016;144:1-13.

[15] Castanié B, Bouvet C, Aminanda Y, Barrau JJ, Thevenet P. Modelling of low-energy/low-velocity impact on Nomex honeycomb sandwich structures with metallic skins. International Journal of Impact Engineering. 2008;35:620-634.

[16] Tounsi R, Zouari B, Chaari F, Markiewicz E, Haugou G, Dammak F. Reduced numerical model to investigate the dynamic behaviour of honeycombs under mixed shear-compression loading. Thin-Walled Structures. 2013;73:290-301.

[17] Zhang X, Zhang H, Wen Z. Experimental and numerical studies on the crush resistance of aluminum honeycombs with various cell configurations. International Journal of Impact Engineering. 2014;66:48-59.

[18] Yamashita M, Gotoh M. Impact behavior of honeycomb structures with various cell specifications - Numerical simulation and experiment. International Journal of Impact Engineering. 2006;32:618-630.

[19] Juan Carlos Álvarez E, Andrés Díaz L. Comparative study of auxetic geometries by means of computer-aided design and engineering. Smart Materials and Structures. 2012;21:105004.

[20] LAKERS RS. Making and characterizing negative Poisson's ratio materials. International Journal of Mechanical Engineering Education. 2000;30:50-58.

[21] Saxena KK, Das R, Calius EP. Three Decades of Auxetics Research − Materials with Negative Poisson's Ratio: A Review. Advanced Engineering Materials. 2016;18:1847-1870.

[22] Zhang XC, An LQ, Ding HM, Zhu XY, El-Rich M. The influence of cell micro-structure on the in-plane dynamic crushing of honeycombs with negative Poisson's ratio. Journal of Sandwich Structures and Materials. 2015;17:26-55.

[23] Evans KE, Nkansah MA, Hutchinson IJ, Rogers SC. Molecular network design. Nature. 1991;353:124-124.

[24] Timoshenko SP, Goodier JN. Theory of Elasticity. 3 ed. New York: McGraw Hill, 1970.

[25] Evans KE, Alderson A. Auxetic materials: Functional materials and structures from lateral thinking! Advanced Materials. 2000;12:617-628.

[26] Liu W, Wang N, Luo T, Lin Z. In-plane dynamic crushing of re-entrant auxetic cellular structure. Materials & Design. 2016;100:84-91.

[27] Hassan MR, Scarpa F, Ruzzene M, Mohammed NA. Smart shape memory alloy chiral honeycomb. Materials Science and Engineering A. 2008;481-482:654-657.

[28] Bettini P, Airoldi A, Sala G, Landro LD, Ruzzene M, Spadoni A. Composite chiral structures for morphing airfoils: Numerical analyses and development of a manufacturing process. Composites Part B: Engineering. 2010;41:133-147.

[29] Tee KF, Spadoni A, Scarpa F, Ruzzene M. Wave propagation in auxetic tetrachiral honeycombs. Journal of Vibration and Acoustics, Transactions of the ASME. 2010;132:0310071-0310078.

[30] Strek T, Michalski J, Jopek H. Computational Analysis of the Mechanical Impedance of the Sandwich Beam with Auxetic Metal Foam Core. physica status solidi (b). 2019;256:1800423.

[31] Lim TC. Mechanics of Metamaterials with Negative Parameters: Springer Nature Singapore Pte Ltd, 2020.

[32] Lim TC. Auxetic Materials and Structures. Singapore Springer, 2015.

[33] Jopek H, Stręk T. Thermoauxetic Behavior of Composite Structures. 2018;11:294.

[34] Critchley R, Corni I, Wharton JA, Walsh FC, Wood RJK, Stokes KR. A review of the manufacture, mechanical properties and potential applications of auxetic foams. physica status solidi (b). 2013;250:1963-1982.

[35] Scarpa F, Alderson A, Ruzzene M, Wojciechowski K. Auxetics in smart systems and structures 2015. Smart Materials and Structures. 2016;25:050301.

[36] Novak N, Vesenjak M, Ren Z. Auxetic Cellular Materials - a Review. Strojniski Vestnik / Journal of Mechanical Engineering. 2016;62:485-493.

[37] Yang W, Li Z-M, Shi W, Xie B-H, Yang M-B. Review on auxetic materials. Journal of materials science. 2004;39:3269-3279.

[38] Wu W, Hu W, Qian G, Liao H, Xu X, Berto F. Mechanical design and multifunctional applications of chiral mechanical metamaterials: A review. Materials & Design. 2019;180:107950.

[39] Prawoto Y. Seeing auxetic materials from the mechanics point of view: A structural review on the negative Poisson's ratio. Computational Materials Science. 2012;58:140-153.

[40] Lakes RS. Negative-Poisson's-Ratio Materials: Auxetic Solids. Annual Review of Materials Research. 2017;47:63-81.

[41] Huang C, Chen L. Negative Poisson's Ratio in Modern Functional Materials. Advanced Materials. 2016;28:8079-8096.

[42] Evans KE. Auxetic polymers: a new range of materials. Endeavour. 1991;15:170-174.

[43] Alderson A, Alderson KL, Attard D, Evans KE, Gatt R, Grima JN, et al. Elastic constants of 3-, 4- and 6-connected chiral and anti-chiral honeycombs subject to uniaxial in-plane loading. Composites Science and Technology. 2010;70:1042-1048.

[44] Chen YJ, Scarpa F, Liu YJ, Leng JS. Elasticity of anti-tetrachiral anisotropic lattices. International Journal of Solids and Structures. 2013;50:996-1004.

[45] Mousanezhad D, Haghpanah B, Ghosh R, Hamouda AM, Nayeb-Hashemi H, Vaziri A. Elastic properties of chiral, anti-chiral, and hierarchical honeycombs: A simple energy-based approach. Theoretical and Applied Mechanics Letters. 2016;6:81-96.

[46] Imbalzano G, Tran P, Ngo TD, Lee PVS. A numerical study of auxetic composite panels under blast loadings. Composite Structures. 2016;135:339-352.

[47] Wu X, Su Y, Shi J. In-plane impact resistance enhancement with a graded cell-wall angle design for auxetic metamaterials. Composite Structures. 2020;247:112451.

[48] Logakannan KP, Ramachandran V, Rengaswamy J, Ruan D. Dynamic Performance of a 3D Re-entrant Structure. Mechanics of Materials. 2020;148:103503.

[49] Yu R, Luo W, Yuan H, Liu J, He W, Yu Z. Experimental and numerical research on foam filled re-entrant cellular structure with negative Poisson's ratio. Thin-Walled Structures. 2020;153:106679.

[50] Zhang G, Ghita OR, Evans KE. Dynamic thermo-mechanical and impact properties of helical auxetic yarns. Composites Part B: Engineering. 2016;99:494-505.

[51] Yuanlong W, Liangmo W, Zheng-dong M, Tao W. Parametric analysis of a cylindrical negative Poisson's ratio structure. Smart Materials and Structures. 2016;25:035038.

[52] Mohsenizadeh S, Alipour R, Ahmad Z, Alias A. Influence of auxetic foam in quasi-static axial crushing. International Journal of Materials Research. 2016;107:916-924.

[53] Mohsenizadeh S, Alipour R, Shokri Rad M, Farokhi Nejad A, Ahmad Z. Crashworthiness assessment of auxetic foam-filled tube under quasi-static axial loading. Materials & Design. 2015;88:258-268.

[54] Mohsenizadeh S, Alipour R, Nejad AF, Rad MS, Ahmad Z. Experimental Investigation on Energy Absorption of Auxetic Foam-filled Thin-walled Square Tubes under Quasi-static Loading. Procedia Manufacturing. 2015;2:331-336.

[55] Prall D, Lakes RS. Properties of a chiral honeycomb with a poisson's ratio of — 1. International Journal of Mechanical Sciences. 1997;39:305-314.

[56] Spadoni A, Ruzzene M. Elasto-static micropolar behavior of a chiral auxetic lattice. Journal of the Mechanics and Physics of Solids. 2012;60:156-171.

[57] Spadoni A. Application of chiral cellular materials for the design of innovative components: Georgia Institute of Technology, 2008.

[58] Spadoni A, Ruzzene M, Scarpa F. Global and local linear buckling behavior of a chiral cellular structure. Physica Status Solidi (B) Basic Research. 2005;242:695-709.

[59] Haghpanah B, Papadopoulos J, Mousanezhad D, Nayeb-Hashemi H, Vaziri A. Buckling of regular, chiral and hierarchical honeycombs under a general macroscopic stress state. Proceedings of the Royal Society A: Mathematical, Physical and Engineering Sciences. 2014;470.

[60] Pozniak AA, Wojciechowski KW. Poisson's ratio of rectangular anti-chiral structures with size dispersion of circular nodes. Physica Status Solidi (B) Basic Research. 2014;251:367-374.

[61] Cicala G, Recca G, Oliveri L, Perikleous Y, Scarpa F, Lira C, et al. Hexachiral truss-core with twisted hemp yarns: Out-of-plane shear properties. Composite Structures. 2012;94:3556-3562.

[62] Miller W, Smith CW, Scarpa F, Evans KE. Flatwise buckling optimization of hexachiral and tetrachiral honeycombs. Composites Science and Technology. 2010;70:1049-1056.

[63] Scarpa F, Blain S, Lew T, Perrott D, Ruzzene M, Yates JR. Elastic buckling of hexagonal chiral cell honeycombs. Composites Part A: Applied Science and Manufacturing. 2007;38:280-289.

[64] Lorato A, Innocenti P, Scarpa F, Alderson A, Alderson KL, Zied KM, et al. The transverse elastic properties of chiral honeycombs. Composites Science and Technology. 2010;70:1057-1063.

[65] Gao D, Zhang C. Theoretical and numerical investigation on in-plane impact performance of chiral honeycomb core structure. Journal of Structural Integrity and Maintenance. 2018;3:95-105.

[66] Mousanezhad D, Ghosh R, Ajdari A, Hamouda AMS, Nayeb-Hashemi H, Vaziri A. Impact resistance and energy absorption of regular and functionally graded hexagonal honeycombs with cell wall material strain hardening. International Journal of Mechanical Sciences. 2014;89:413-422.

[67] SIMULIA. Abaqus Analysis User's Guide Version 6.14. Dassault Systèmes Simulia Corp., Providence, RI, USA.; 2014.

[68] Zhao H, Gary G. Crushing behaviour of aluminium honeycombs under impact loading. International Journal of Impact Engineering. 1998;21:827-836.

[69] Chen Y, Clausen AH, Hopperstad OS, Langseth M. Stress–strain behaviour of aluminium alloys at a wide range of strain rates. International Journal of Solids and Structures. 2009;46:3825-3835.

[70] Ajdari A, Nayeb-Hashemi H, Vaziri A. Dynamic crushing and energy absorption of regular, irregular and functionally graded cellular structures. International Journal of Solids and Structures. 2011;48:506-516.

Declaration of interests

☐The authors declare the following financial interests/personal relationships which may be considered as potential competing interests:

Author Statement

Dianwei Gao: Methodology, Visualization, Investigation, Data curation, Formal analysis, Writing - original draft, Writing - review & editing. **Shuhong Wang:** Supervision, Funding acquisition, Resources. **Mingzhong Zhang:** Supervision, Validation. **Chunwei Zhang:** Conceptualization, Funding acquisition, Resources, Supervision.